

See discussions, stats, and author profiles for this publication at: <https://www.researchgate.net/publication/51859094>

# Enhancement of the Visible-Light Photocatalytic Activity of In<sub>2</sub>O<sub>3</sub>-TiO<sub>2</sub> Nanofiber Heteroarchitectures

ARTICLE in ACS APPLIED MATERIALS & INTERFACES · DECEMBER 2011

Impact Factor: 6.72 · DOI: 10.1021/am201499r · Source: PubMed

CITATIONS

93

READS

125

9 AUTHORS, INCLUDING:



Mingyi Zhang

Harbin Normal University

60 PUBLICATIONS 1,776 CITATIONS

SEE PROFILE



Peng Zhang

Northeast Normal University

31 PUBLICATIONS 1,329 CITATIONS

SEE PROFILE



Zhenyi Zhang

Dalian Nationalities University

46 PUBLICATIONS 1,946 CITATIONS

SEE PROFILE

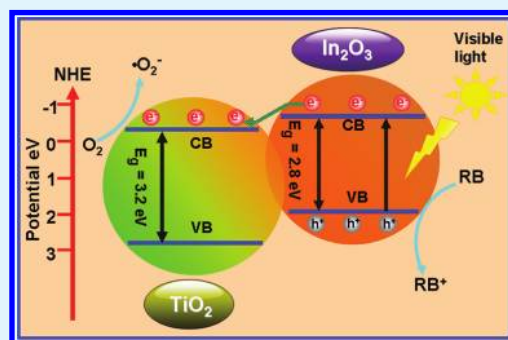
# Enhancement of the Visible-Light Photocatalytic Activity of $\text{In}_2\text{O}_3$ – $\text{TiO}_2$ Nanofiber Heteroarchitectures

Jingbo Mu,<sup>†</sup> Bin Chen,<sup>\*,†</sup> Mingyi Zhang,<sup>‡</sup> Zengcai Guo,<sup>†</sup> Peng Zhang,<sup>‡</sup> Zhenyi Zhang,<sup>‡</sup> Yangyang Sun,<sup>‡</sup> Changlu Shao,<sup>\*,‡</sup> and Yichun Liu<sup>‡</sup>

<sup>†</sup>Department of Chemistry and <sup>‡</sup>Center for Advanced Optoelectronic Functional Materials Research, and Key Laboratory of UV Light-Emitting Materials and Technology of Ministry of Education, Northeast Normal University, 5268 Renmin Street, Changchun 130024, People's Republic of China

**ABSTRACT:** One-dimensional  $\text{In}_2\text{O}_3$ – $\text{TiO}_2$  heteroarchitectures with high visible-light photocatalytic activity have been successfully obtained by a simple combination of electrospinning technique and solvothermal process. The as-obtained products were characterized by field emission scanning electron microscopy (FE-SEM), energy-dispersive X-ray (EDX) spectroscopy, transmission electron microscopy (TEM), X-ray diffraction (XRD), X-ray photoelectron spectroscopy (XPS), and UV–vis spectra. The results revealed that the secondary  $\text{In}_2\text{O}_3$  nanostructures were successfully grown on the primary  $\text{TiO}_2$  nanofibers substrates. Compared with the pure  $\text{TiO}_2$  nanofibers, the obtained  $\text{In}_2\text{O}_3$ – $\text{TiO}_2$  heteroarchitectures showed enhancement of the visible-light photocatalytic activity to degrade rhodamine B (RB) because of the formation of heteroarchitectures, which might improve the separation of photogenerated electrons and holes derived from the coupling effect of  $\text{TiO}_2$  and  $\text{In}_2\text{O}_3$  heteroarchitectures. Moreover, the  $\text{In}_2\text{O}_3$ – $\text{TiO}_2$  heteroarchitectures could be easily recycled without the decrease in the photocatalytic activity because of their one-dimensional nanostructural property.

**KEYWORDS:**  $\text{In}_2\text{O}_3$ ,  $\text{TiO}_2$ , heteroarchitectures, photocatalysis, degradation



## 1. INTRODUCTION

With the development of industry and economy of human society, environmental problems are becoming more and more serious. Since Fujishima and Honda reported the evolution of oxygen and hydrogen from a  $\text{TiO}_2$  electrode under the irradiation of light in 1972,<sup>1</sup> photocatalysis was regarded as one of the most effective and economical ways to solve the environmental problems. Thus, in recent years, many kinds of semiconductor metal oxide photocatalyst, such as  $\text{Bi}_2\text{O}_3$ ,  $\text{Fe}_2\text{O}_3$ ,  $\text{ZnO}$ ,  $\text{TiO}_2$  and so forth, have been developed for creating a comfortable environment for human beings.<sup>2–7</sup> In particular, titanium dioxide ( $\text{TiO}_2$ ) has been widely studied as a semiconductor photocatalyst for potential application in air purification and photocatalytic degradation of organic pollutants owing to its excellent (photo) chemical stability, low cost and nontoxicity.<sup>8–13</sup> However, the application of  $\text{TiO}_2$  is limited by its large band gap energy (3.2 eV for anatase), which limits its photoresponse only to the ultraviolet (UV) region. Unfortunately, only a small ultraviolet (UV) fraction (<4%) of the total solar spectrum reaching the surface of the earth.<sup>14</sup> Therefore, how to make  $\text{TiO}_2$  responsive to visible light in photocatalysis becomes an important subject for developing the  $\text{TiO}_2$ -based photocatalysts. In the past decade, many attempts have been made to extend the photoresponse of the  $\text{TiO}_2$  to visible region.<sup>15–27</sup> Among these attempts,  $\text{TiO}_2$  doping with transition metals ions or nonmetal elements, such as V, Co, Fe, C, N, S, or I, has been a common approach for improving the

photocatalytic performance of the catalyst.<sup>28,29</sup> Although the above modifications could partly improve the photocatalytic activity of  $\text{TiO}_2$ , some key problems remain unresolved, for example, doped materials suffer from thermal instability, photo corrosion, lattice distortion, and an increase in the carrier-recombination probability.<sup>30</sup> One of the promising strategies to overcome this drawback is to couple  $\text{TiO}_2$  with other narrow band gap semiconductors serving as the sensitizer to absorb visible light.

$\text{In}_2\text{O}_3$ , an indirect band semiconductor with a direct band gap of 3.6 eV and an indirect band gap of 2.8 eV,<sup>31</sup> had proved to be an efficient sensitizer to extend the absorption spectra of oxide semiconductor photocatalysts from the UV region into the visible region.<sup>32–34</sup> Moreover, the coupling of two different semiconductors could transfer electrons from an excited small band gap semiconductor into another attached one in the case of proper conduction band potentials. This favors the separation of photoinduced electrons and holes and thus improved the photocatalytic efficiency of semiconductor heterostructure dramatically. Considering the band gap of  $\text{In}_2\text{O}_3$  ( $E_g = 2.8$  eV) is lower than that of  $\text{TiO}_2$  ( $E_g = 3.0$  eV for rutile,  $E_g = 3.2$  eV for anatase), but the conduction band (CB) of  $\text{In}_2\text{O}_3$  ( $E_{CB}$  for  $\text{In}_2\text{O}_3 = -0.63$  V versus NHE) is higher than

Received: October 29, 2011

Accepted: December 12, 2011

Published: December 12, 2011

that of  $\text{TiO}_2$  ( $E_{\text{CB}}$  for  $\text{TiO}_2 = -0.4$  V versus NHE), an efficient heterostructure could be formed for the separation of photogenerated charge carriers when coupling them together. Recently, a rich variety of  $\text{In}_2\text{O}_3$ - $\text{TiO}_2$  photocatalysts have been prepared, including nanoparticles, films, and so on.<sup>35–40</sup> Among these materials, the  $\text{In}_2\text{O}_3$ - $\text{TiO}_2$  nanopowders exhibit a high photocatalytic activity because of their high surface area. However, it is often limited, because the suspended particulate catalysts are easily lost in the process of photocatalytic reaction and separation, which may repollute the treated water again. Meanwhile, the  $\text{In}_2\text{O}_3$ - $\text{TiO}_2$  films can be fixed and reclaimed easily, but their photocatalytic activity is decreased because of their low surface area. Compared with the corresponding nanoparticles and thin films of  $\text{In}_2\text{O}_3$ - $\text{TiO}_2$ , the one-dimensional nanomaterials of the  $\text{In}_2\text{O}_3$ - $\text{TiO}_2$  possessed high photocatalytic activity and favorable recycling characteristics due to its high surface area and one-dimensional properties, which might be deemed as potential good candidates for practical application. However, to the best of knowledge, there has been no report on the preparation and photocatalytic properties of these kinds of materials.

Motivated by the above concerns, we fabricate one-dimensional  $\text{In}_2\text{O}_3$ - $\text{TiO}_2$  heteroarchitectures photocatalysts based on  $\text{TiO}_2$  nanofibers by combining the electrospinning technique with the solvothermal method. And the photocatalytic activity of these heteroarchitectures photocatalysts in the visible-light region are investigated by measuring the degradation of dye RB as a test substance. The experimental results showed that the as-obtained  $\text{In}_2\text{O}_3$ - $\text{TiO}_2$  heteroarchitectures exhibited excellent visible light photocatalytic activity. Moreover, due to the large length to diameter ratio of  $\text{TiO}_2$  nanofibers, the  $\text{In}_2\text{O}_3$ - $\text{TiO}_2$  heteroarchitectures could be reclaimed easily by sedimentation without a decrease of the photocatalytic activity. Finally, the mechanisms of visible photocatalysis in  $\text{In}_2\text{O}_3$ - $\text{TiO}_2$  heteroarchitectures were proposed.

## 2. MATERIALS AND METHODS

**2.1. Preparation of  $\text{TiO}_2$  Nanofibers.** First, 2 g of poly(vinylpyrrolidone) powder (PVP,  $M_w = 1\,300\,000$ ) was added to a mixture of 9 mL of absolute ethanol and 5 mL of acetic acid in a capped bottle. The obtained solution was stirred for 1 h to generate a homogeneous solution. Then, 2.0 g  $\text{Ti}(\text{OC}_4\text{H}_9)_4$  was added to the solution, and the mixture was continuously stirred for another 1 h to make precursor solution. Three milliliters of the precursor solution was placed in a 5 mL syringe equipped with a blunt metal needle of 0.8 mm outer diameter and 0.6 mm inner diameter. A stainless steel plate covered with a sheet of aluminum foil was employed as the collector. The distance between the needle tip and collector was 15 cm, and the voltage was set at 9 kV. The as-collected nanofibers were calcined at 550 °C for 2 h to form anatase  $\text{TiO}_2$  nanofibers.

**2.2. Fabrication of  $\text{In}_2\text{O}_3$ - $\text{TiO}_2$  Heteroarchitectures.** In a typical experiment, 0.3 mmol  $\text{In}(\text{NO}_3)_3 \cdot 5\text{H}_2\text{O}$ , 1 g  $\text{CO}(\text{NH}_2)_2$  were dissolved in the mixture of 13 mL of diethylene glycol (DEG) and 2 mL of  $\text{H}_2\text{O}$  under magnetic stirring. The resulting solution and the obtained  $\text{TiO}_2$  (15 mg) was transferred into a 20 mL Teflon-lined stainless autoclave, sealed and maintained at 200 °C for 24 h, and then cooled down to room temperature. The as-fabricated products were collected out, washed several times with ethanol and deionized water, respectively, then dried at 60 °C for 12 h. Thus, the  $\text{In}_2\text{O}_3$ - $\text{TiO}_2$  heteroarchitectures were fabricated, which was denoted as IT1. By this method, the samples IT2 was prepared at the additive amount of  $\text{In}(\text{NO}_3)_3 \cdot 5\text{H}_2\text{O}$  was 0.6 mmol. In addition, for simplicity, pure  $\text{TiO}_2$  nanofibers were denoted as IT0. For contrast, the pure  $\text{In}_2\text{O}_3$  was

obtained in the absence of  $\text{TiO}_2$  during the process of preparation of the  $\text{In}_2\text{O}_3$ - $\text{TiO}_2$  heteroarchitectures and ready for further test.

**2.3. Characterization.** The scanning electron microscopy (SEM, XL-30 ESEM FEG, Micro FEI Philips) and transmission electron microscopy (TEM; high resolution TEM [HRTEM], JEM-3010) were used to characterize the morphologies of the products. Energy dispersive X-ray (EDX) spectroscopy being attached to scanning electron microscopy (SEM) was used to analyze the composition of samples. X-ray diffraction (XRD) measurement was carried out using a D/max 2500 XRD spectrometer (Rigaku) with Cu K $\alpha$  line of 0.1541 nm. X-ray photoelectron spectroscopy (XPS) was performed on a VG ESCALAB LKII instrument with Mg K $\alpha$ -ADES ( $h\nu = 1253.6$  eV) source at a residual gas pressure of below  $1 \times 10^{-8}$  Pa. The UV–vis diffuse reflectance (DR) spectroscopy of the samples were recorded on a Cary 500 UV–vis–NIR spectrophotometer for wavelengths from 200 to 800 nm (the irradiation time was 40 s). The photoluminescence (PL) spectra of photocatalysts were detected with a Jobin Yvon HR800 micro-Raman spectrometer using a 325 nm line from a He–Cd laser. The specific surface areas of the samples were measured with a Micromeritics ASAP 2010 instrument and analyzed by the BET method.

**2.4. Photocatalytic test.** The photoreactor was designed with an internal xenon lamp (XHA 150W) equipped with a cutoff glass filter transmitting  $\lambda > 420$  nm surrounded by a water-cooling quartz jacket to cool the lamp, where a 100 mL of the RB solution with an initial concentration of 10 mg  $\text{L}^{-1}$  in the presence of solid catalyst (0.05 g). The solution was stirred in the dark for 30 min to obtain a good dispersion and establish adsorption–desorption equilibrium between the organic molecules and the catalyst surface. Decreases in the concentrations of dyes were analyzed by a Cary 500 UV–vis–NIR spectrophotometer. At given intervals of illumination, the samples of the reaction solution were taken out and then centrifuged and filtered. Finally, the filtrates were analyzed.

## 3. RESULTS AND DISCUSSIONS

The morphology of the samples were observed by FESEM, which were shown in Figure 1. Figure a1 and a2 showed the

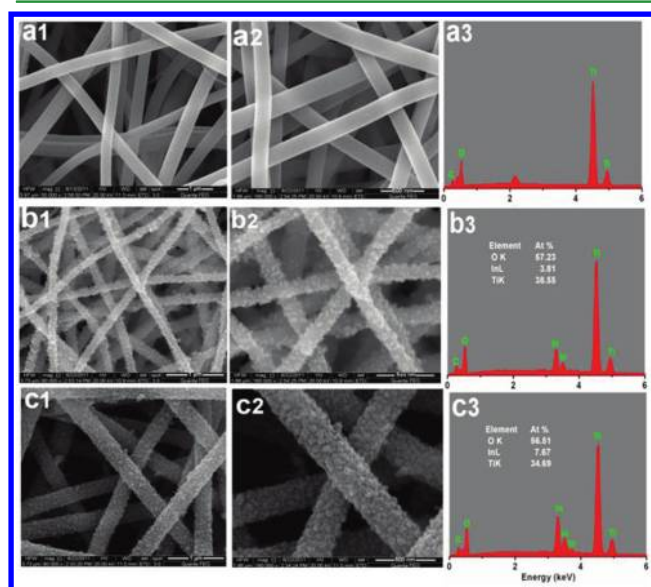


**Figure 1.** (a1, a2) SEM images of sample IT0 with different magnifications; (b1, b2) SEM images of sample IT1 with different magnifications; (c1, c2) SEM images of sample IT2 with different magnifications; (a3) EDX spectrum of sample IT0; (b3) EDX spectra of sample IT1 and IT2 (c3).

typical SEM images of the electrospun  $\text{TiO}_2$  nanofibers before solvothermal treatment. From image a1, it could be observed



that the pure  $\text{TiO}_2$  aligned in random orientation because of the bending instability associated with the spinning jet. Image a2 displays the corresponding SEM image with higher magnification. It was showed that these randomly oriented  $\text{TiO}_2$  had a smooth and uniform surface without secondary nanostructures, and the diameter of the  $\text{TiO}_2$  ranged from 120 to 250 nm. After solvothermal treatment, the as-fabricated sample remained as a nonwoven nanofibrous morphology, as shown in image b1. However, the surface of the  $\text{TiO}_2$  was no longer smooth. Instead, the nanofibers were decorated with numerous secondary nanoparticles. Image b2 was the higher-magnification image of the sample IT1, it could be observed that the nanoparticles were uniformly distributed across the surface of each fiber, offering the high level exposure of the nanoparticles' surface. Images c1 and c2 revealed the different magnified image of sample IT2. It could be observed that the density of the nanoparticles was dramatically increased when the precursor molar ratio of reactants was increased. It was worth pointing out that the surface area of  $\text{TiO}_2$  was advantageous for uniform growth and distribution of  $\text{In}_2\text{O}_3$  nanoparticles on the surface of  $\text{TiO}_2$ . Images a3, b3, and c3 were the energy-dispersive X-ray (EDX) spectrum of the samples  $\text{TiO}_2$ , IT1 and IT2, respectively. It was indicated that C, O and Ti elements existed in pure electropun  $\text{TiO}_2$ , while C, O, Ti and In existed in the  $\text{In}_2\text{O}_3$ - $\text{TiO}_2$  heteroarchitectures (IT1 and IT2), respectively. C peaks in images a3, b3, and c3 were attributed to the FESEM platform used to support the nanofibers. The EDX analysis results showed that the atomic ratios of In to Ti were about 1/10 and 11/50 for IT1 and IT2, respectively. Accordingly, the mass percentage of  $\text{In}_2\text{O}_3$  in the  $\text{In}_2\text{O}_3$ - $\text{TiO}_2$  heteroarchitectures could be determined as 15 and 28% for IT1 and IT2, respectively. The EDX spectra further confirmed that the  $\text{In}_2\text{O}_3$ - $\text{TiO}_2$  heteroarchitectures were successfully fabricated.

To obtain the microstructure of the  $\text{In}_2\text{O}_3$ - $\text{TiO}_2$  heteroarchitectures, the TEM images depicted in Figure 2 provided a

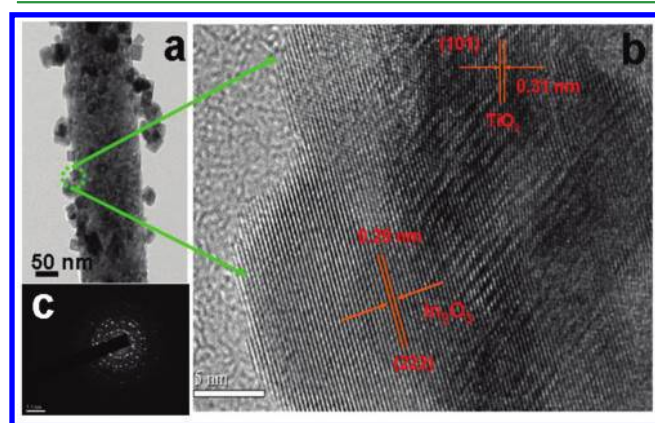


**Figure 2.** (a) TEM image of the sample IT1. (b) HRTEM image of the sample IT1. (c) SAED pattern of sample IT1.

clear observation of the as-synthesized IT1 sample. The low magnification TEM image of the  $\text{In}_2\text{O}_3$ - $\text{TiO}_2$  heteroarchitectures was displayed in Figure 2a. It could be seen that the ultrasonic process during the sample preparation for TEM measurements did not caused the  $\text{In}_2\text{O}_3$  nanoparticles to fall off the  $\text{TiO}_2$ , it indicated that  $\text{In}_2\text{O}_3$  nanoparticles had been successfully grown onto the surface of the  $\text{TiO}_2$ . Moreover, it could be observed that the diameter of  $\text{TiO}_2$  was about 130 nm,

which was in agreement with the SEM analysis above. And the  $\text{In}_2\text{O}_3$  nanoparticles possessed the average size about 20–30 nm. Meanwhile, a high-resolution image of the  $\text{In}_2\text{O}_3$ - $\text{TiO}_2$  heteroarchitectures obtained from the area marked with a circularity in Figure 2a were shown in Figure 2b. The junction displayed two types of clear lattice fringes as shown in Figure 2b, one set of the fringes spacing was *ca.* 0.31, corresponding to the (101) plane of the anatase crystal structure of  $\text{TiO}_2$ . Another set of the clear fringes spacing measures *ca.* 0.29 nm, which corresponded to the (222) lattice spacing of the cubic phase of  $\text{In}_2\text{O}_3$ . In Figure 2c, the corresponding ringlike selected-area electron diffraction (SAED) pattern indicated the nanoparticles had a polycrystalline structure. These results confirmed that the heteroarchitectures were well-formed between  $\text{TiO}_2$  nanoparticles and  $\text{In}_2\text{O}_3$ .

The X-ray diffraction (XRD) patterns of the as-obtained samples IT1, IT2 and pure  $\text{TiO}_2$  were shown in Figure 3.

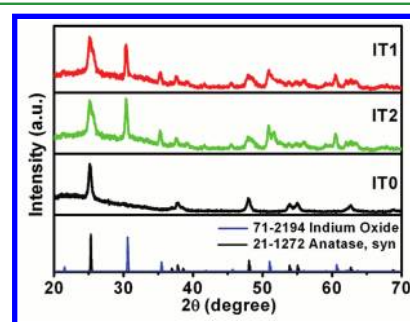


**Figure 3.** XRD patterns of  $\text{In}_2\text{O}_3$ - $\text{TiO}_2$  heteroarchitectures (IT1, IT2) and pure  $\text{TiO}_2$  nanofibers (IT0).

The curve a in Figure 1 revealed that the crystal phase of  $\text{TiO}_2$  nanofibers was anatase with the diffraction peaks at about  $2\theta = 25.5, 37.9, 48.2, 54.1, 55.0,$  and  $62.8^\circ$ , which could be perfectly indexed to the (101), (004), (200), (105), (211) and (204) crystal faces of anatase  $\text{TiO}_2$  (PDF card 21-1272, JCPDS). After solvothermal treatment at  $200^\circ\text{C}$  for 24 h, as shown in samples IT1 and IT2, additional diffraction peaks with  $2\theta$  values of  $30.42, 35.28, 50.94,$  and  $60.52^\circ$  appeared, which could be perfectly indexed to the (222), (400), (440), and (622) crystal planes of the body-centered cubic (bcc)  $\text{In}_2\text{O}_3$  crystalline phase with a lattice constant of  $a = 10.1 \text{ \AA}$  (PDF card 71-2194, JCPDS). No characteristic peaks for impurity, such as In,  $\text{In}(\text{OH})_3$  or  $\text{InTiO}_5$  were observed, suggesting that the composition of the above nanofibers was  $\text{In}_2\text{O}_3$  and  $\text{TiO}_2$ . Moreover, the average grain sizes of the products was calculated by applying the Debye-Scherrer formula,  $D = K\lambda/(\beta\cos\theta)$ , where  $\lambda$  was the wavelength of the X-ray radiation ( $\text{Cu K}\alpha = 0.15406 \text{ nm}$ ),  $K$  was a constant taken as 0.89,  $\beta$  was the line width at half-maximum height, and  $\theta$  was the diffracting angle. The average particle size had been calculated using the three different prominent planes of (222), (400), and (440) with mean values of 28.89 and 35.26 nm for IT1 and IT2, respectively. It was worthwhile to note that the diffraction peaks of  $\text{In}_2\text{O}_3$  in IT1 and IT2 were sharp and intense, implying the high crystallinity of the  $\text{In}_2\text{O}_3$  nanocubes in the  $\text{In}_2\text{O}_3$ - $\text{TiO}_2$  heteroarchitectures.

To confirm the chemical composition and purity of the prepared heteroarchitectures, the sample IT1 was further studied and compared with those of the pure  $\text{TiO}_2$  nanofibers (IT0) by XPS analysis. The fully scanned spectra (Figure 4a) showed that elements In, Ti, O and C existed in  $\text{In}_2\text{O}_3$ - $\text{TiO}_2$

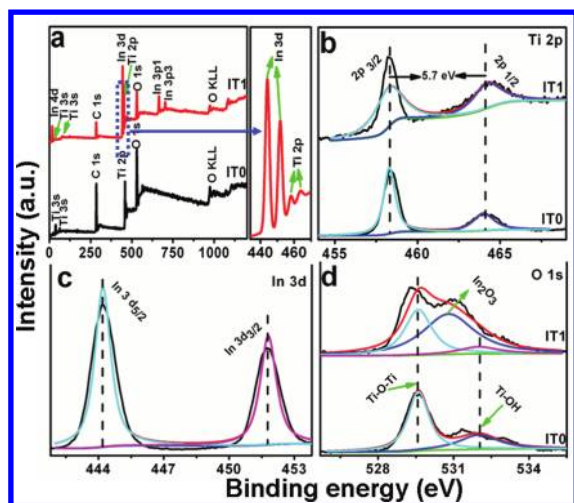


**Figure 4.** (a) XPS fully scanned spectra of the typical  $\text{In}_2\text{O}_3$ - $\text{TiO}_2$  heteroarchitectures (IT1) and pure  $\text{TiO}_2$  nanofibers (IT0); (b) XPS spectra of Ti 2p for the typical  $\text{In}_2\text{O}_3$ - $\text{TiO}_2$  heteroarchitectures (IT1) and pure  $\text{TiO}_2$  nanofibers (IT0); (c) XPS spectrum of In 3d for the  $\text{In}_2\text{O}_3$ - $\text{TiO}_2$  heteroarchitectures (IT1); (d) XPS spectra of O 1s for  $\text{In}_2\text{O}_3$ - $\text{TiO}_2$  heteroarchitectures (IT1) and pure  $\text{TiO}_2$  nanofibers (IT0).

heteroarchitectures, while, Ti, O and C elements existed in bare  $\text{TiO}_2$  nanofibers, respectively. The C element could be ascribed to the adventitious carbon-based contaminant, and the binding energy for C 1s peak at 284.6 eV was used as the reference for calibration. The high-resolution XPS spectra with scanning over the area corresponding to the binding energies for the Ti 2p region around 460 eV were analyzed in Figure 4b. For the sample IT1, the peak located at 464.2 eV corresponds to the  $\text{Ti } 2p_{1/2}$  and another one located at 458.5 eV was assigned to  $\text{Ti } 2p_{3/2}$ . The splitting between  $\text{Ti } 2p_{1/2}$  and  $\text{Ti } 2p_{3/2}$  was 5.7 eV, indicating a normal state of  $\text{Ti}^{4+}$  in the  $\text{In}_2\text{O}_3$ - $\text{TiO}_2$  heteroarchitectures. Besides, the peaks for Ti 2p in the sample IT1 showed no shift compared with that in pure  $\text{TiO}_2$  nanofibers, confirming that the structure of  $\text{TiO}_2$  remained intact after synthesis of  $\text{In}_2\text{O}_3$ - $\text{TiO}_2$  heteroarchitectures. Figure 4c revealed the high resolution XPS spectra for the In 3d, because of the spin-orbital splits, the In  $3d_{5/2}$  and In  $3d_{3/2}$  XPS peaks also had characteristic double peaks centered at binding energies of 444.2 and 451.8 eV, respectively. Compared with the reported In  $3d_{5/2}$  signal of metallic indium, which appeared at 443.6 eV, the absence of this peak excluded the existence of metallic indium, and indicated that in the element indium in  $\text{In}_2\text{O}_3$ - $\text{TiO}_2$  heteroarchitectures existed in the oxide state only.<sup>41</sup> The O 1s XPS spectrum could be resolved using the XPS peak fitting program, version 4.1. Figure 4d presented the O 1s photoelectron peaks. For the pure  $\text{TiO}_2$  nanofibers (IT0), there existed only two oxygen signals, at 529.6 and 532 eV, that were attributed to Ti-O-Ti (lattice O) and Ti-OH, respectively,<sup>42</sup> whereas for the  $\text{In}_2\text{O}_3$ - $\text{TiO}_2$  heteroarchitectures (IT1), obviously, a new oxygen signal at 530.7 eV appeared that could be indexed to oxygen anions from indium oxide.<sup>43</sup> All of these results gave the insight that the heteroarchitectures were composed of  $\text{In}_2\text{O}_3$  and  $\text{TiO}_2$ . The relative quantitative analysis of each element was completed using the XPS peak area data of different elements and their respective elemental sensitivity factor according to the equation below

$$n(E1)/n(E2) = [A(E1)/S(E1)]/[A(E2)/S(E2)] \quad (1)$$

where  $n$  was the number of the atom,  $E_i$  was the element  $i$ ,  $A$  was the peak area, and  $S$  was the elemental sensitivity factor.<sup>44</sup> The sensitive factor  $S$  of In  $3d_{5/2}$  and Ti 2p was 3.77, and 1.80, respectively. Here, the molar ratio of Ti to In was 19.8:2.1. The result showed that the value calculated was close to the EDX analyses.

The diffuse reflectance spectra for the synthesized  $\text{In}_2\text{O}_3$ - $\text{TiO}_2$  heteroarchitectures were presented in Figure 5.

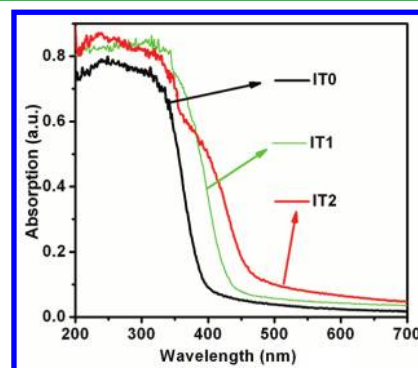


**Figure 5.** UV-vis spectra of different samples.

For comparison, the spectra of pure  $\text{TiO}_2$  and  $\text{In}_2\text{O}_3$  synthesized under identical conditions were also plotted. As could be seen from the curve of pure  $\text{TiO}_2$  nanofibers,  $\text{TiO}_2$  nanofibers showed a clear absorption edge at about 390 nm, and only exhibited the fundamental absorption in the UV region. For the heteroarchitectures, the curves of samples IT1 and IT2 exhibited the a mixed absorption property of both  $\text{TiO}_2$  and  $\text{In}_2\text{O}_3$ . Moreover, the visible light absorbance was increased with the increase in density of the  $\text{In}_2\text{O}_3$  grown on  $\text{TiO}_2$  nanofibers.

To demonstrate the photoactivity of the as-obtained  $\text{In}_2\text{O}_3$ - $\text{TiO}_2$  heteroarchitectures for the degradation of organic pollutants, we had carried out the experiments of the photocatalytic degradation of rhodamine B (RB) as a test reaction. Furthermore, in the comparative experiments, the pure  $\text{TiO}_2$  (IT0)  $\text{In}_2\text{O}_3$  and the Degussa-P25 were used as a photocatalytic reference to understand the photocatalytic activity of the  $\text{In}_2\text{O}_3$ - $\text{TiO}_2$  heteroarchitectures. The change of absorption spectra of RB aqueous solution showed the change of its concentration. The initial concentration ( $C_0$ ), the final concentration ( $C$ ), and the degradation rate ( $D\%$ ) had a mathematical expression as follows

$$D\% = \frac{C_0 - C}{C_0} 100\% \quad (2)$$

As observed in Figure 6a, the control experiments were performed under different conditions: (1) in the presence of photocatalysts but in the dark and (2) with visible light irradiation but in the absence of the photocatalysts. These control experiments revealed that there was no appreciable degradation of RB over the  $\text{In}_2\text{O}_3$ - $\text{TiO}_2$  heteroarchitectures in the absence of visible light irradiation, indicating that the adsorption of RB on the  $\text{In}_2\text{O}_3$ - $\text{TiO}_2$  heteroarchitectures could be negligible. And, there was no appreciable degradation of RB after 4 h in the absence of photocatalysts. Figure 6b showed the degradation curves of RB on the Degussa-P25,  $\text{In}_2\text{O}_3$ ,  $\text{TiO}_2$  nanofibers, IT1 and IT2. It could be seen that the Degussa-P25 had no photocatalytic activity under the visible light, except



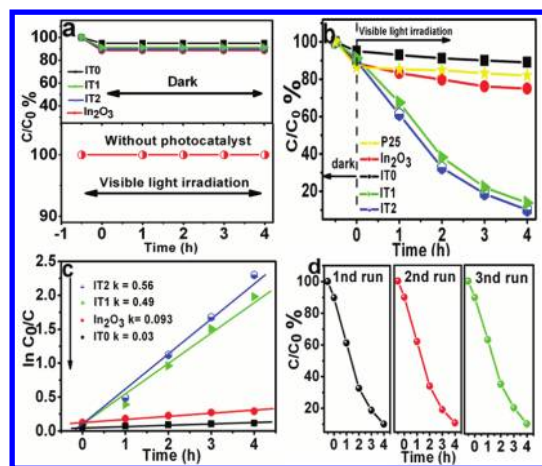


**Figure 6.** (a) Degradation profiles of RB in the presence of the photocatalysts but in the dark and with UV light irradiation but in the absence of the photocatalysts. (b) Degradation profiles of RB over the samples: IT0, IT1, IT2, Degussa-P25 and  $\text{In}_2\text{O}_3$  ( $C_0 = 10$  mg/L, catalyst 0.05 g). (c) Kinetic linear simulation curves of RB photocatalytic degradation with samples: IT0, IT1, IT2 and  $\text{In}_2\text{O}_3$ . (d) Photocatalytic activity of the  $\text{In}_2\text{O}_3$ - $\text{TiO}_2$  heteroarchitectures (IT2) for RB degradation with three times of cycling uses.

decent adsorption for RB, which could be attributed to the high specific surface area of the samples. Meanwhile, only 11% of RB molecular for  $\text{TiO}_2$  and 25% for  $\text{In}_2\text{O}_3$  were decomposed in 4 h. In comparison, after visible light irradiation for 4 h, the degradation efficiency of RB were about 86 and 90% for the IT1 and IT2, respectively. Obviously, the  $\text{In}_2\text{O}_3$ - $\text{TiO}_2$  heteroarchitectures showed much higher photocatalytic activities than that of  $\text{TiO}_2$  and  $\text{In}_2\text{O}_3$ . So RB could be degraded efficiently when visible light was used as the light source in the presence of the  $\text{In}_2\text{O}_3$ - $\text{TiO}_2$  heteroarchitectures photocatalyst. We studied the BET of IT1 and IT2. The surface areas of IT1 and IT2 were 10.83 and 11.59  $\text{m}^2 \text{g}^{-1}$ , respectively. The larger BET surface area could facilitated more efficient contact of the  $\text{In}_2\text{O}_3$ - $\text{TiO}_2$  nanofibers heteroarchitectures with organic contaminants and thus improved its photocatalytic activity. As a result, the photocatalytic activity of IT2 and IT1 were different. The kinetic linear simulation curves of the photocatalytic degradation of RB over the above catalysts showed that the above degradation reactions followed a Langmuir-Hinshelwood apparent first-order kinetics model due to the low initial concentrations of the reactants. The explanation was described below<sup>45</sup>

$$r = \frac{dC}{dt} = \frac{kKC}{(1 + KC)} \quad (3)$$

where  $r$  was the degradation rate of the reactant ( $\text{mg}/(\text{L min})$ ),  $C$  was the concentration of the reactant ( $\text{mg}/\text{L}$ ),  $t$  was the UV light irradiation time,  $k$  was the reaction rate constant ( $\text{mg}/(\text{Lmin})$ ), and  $K$  was the adsorption coefficient of the reactant ( $\text{L}/\text{mg}$ ). When the initial concentration ( $C_0$ ) was very low ( $C_0 = 10$  mg/L for RB in the present experiment), eq 2 could be simplified to an apparent first-order model<sup>46</sup>

$$\ln C_0/C = k_{\text{app}}t = k_{\text{app}}t \quad (4)$$

where  $k_{\text{app}}$  was the apparent first-order rate constant ( $\text{min}^{-1}$ ). The determined  $k_{\text{app}}$  for different catalysts were summarized in Figure 6c. The photocatalytic reactivity order was  $\text{IT2} > \text{IT1} > \text{In}_2\text{O}_3 > \text{IT0}$ . Moreover, the stability of the  $\text{In}_2\text{O}_3$ - $\text{TiO}_2$  heteroarchitectures (IT2) was examined for degradation of RB

during a three cycle experiment, which was very important for the  $\text{In}_2\text{O}_3$ - $\text{TiO}_2$  heteroarchitectures to apply in environmental technology. As shown in Figure 6d, the photocatalytic degradation of RB over the  $\text{In}_2\text{O}_3$ - $\text{TiO}_2$  heteroarchitectures under visible light irradiation was effective. More importantly, it was indicated that these heteroarchitectures nanofibers photocatalysts with high photocatalytic activity could be easily separated and recovered by sedimentation, and would greatly promote their practical application to eliminate the organic pollutants from wastewater.

On the basis of the above results, a proposed mechanism was being discussed to explain the enhancement of the photocatalytic properties of the  $\text{In}_2\text{O}_3$ - $\text{TiO}_2$  heteroarchitectures. The conduction band (CB) bottom and the valence band (VB) top of  $\text{TiO}_2$  lie at  $-0.4$  and  $2.8$  eV with respect to NHE,<sup>47</sup> and the CB bottom and VB top of  $\text{In}_2\text{O}_3$  lie at  $-0.63$  and  $2.17$  eV versus NHE.<sup>32</sup> As illustrated in Figure 7a, both the CB bottom

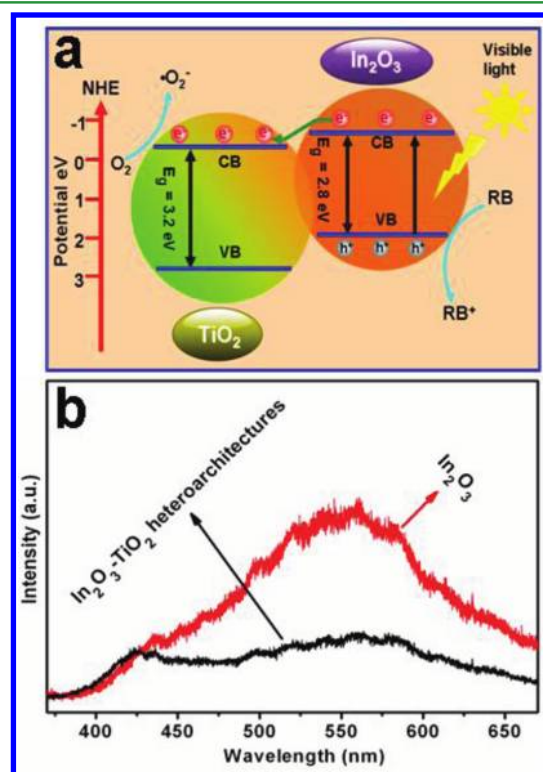
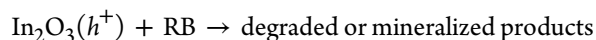
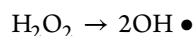
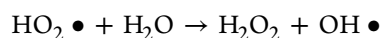
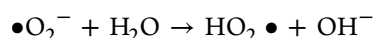
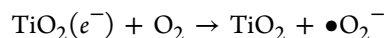
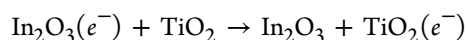
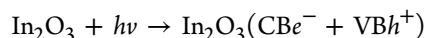


**Figure 7.** (a) Schematic diagram showing the energy band structure and electron-hole pair separation in the  $\text{In}_2\text{O}_3$ - $\text{TiO}_2$  heteroarchitectures. (b) PL emission spectra of  $\text{In}_2\text{O}_3$  and  $\text{In}_2\text{O}_3$ - $\text{TiO}_2$  heteroarchitectures.

and the VB top of  $\text{TiO}_2$  lay below the CB bottom and VB top of  $\text{In}_2\text{O}_3$ , respectively. When they were coupled together to form a heterostructure, the  $\text{In}_2\text{O}_3$  could be excited under visible light irradiation and the generated electrons in the  $\text{In}_2\text{O}_3$  were then migrated to the conduction band (CB) of  $\text{TiO}_2$ . Moreover, due to the high crystallinity of the  $\text{In}_2\text{O}_3$ , the resistance of electron transport was very low and reduced electron-hole recombination. Consequently, the efficient charge separation increased the lifetime of the charge carriers and enhanced the efficiency of the interfacial charge transferred to the adsorbed substrates, leading to higher activity of the  $\text{In}_2\text{O}_3$ - $\text{TiO}_2$  heteroarchitectures photocatalyst. Furthermore, the better separation of photogenerated electrons and holes in the  $\text{In}_2\text{O}_3$ - $\text{TiO}_2$  heteroarchitectures was confirmed by PL emission spectra of

In<sub>2</sub>O<sub>3</sub> and IT2. In Figure 7b, it was indicated that the In<sub>2</sub>O<sub>3</sub>–TiO<sub>2</sub> heteroarchitectures exhibited much lower emission intensity than In<sub>2</sub>O<sub>3</sub>, indicating that the recombination of the photogenerated charge carrier was inhibited greatly in the In<sub>2</sub>O<sub>3</sub>–TiO<sub>2</sub> heteroarchitectures. Since the In<sub>2</sub>O<sub>3</sub> ( $h^+$ ) radicals has a redoxpotential of about 2.17 eV vs NHE, it could oxidize a suitable substrate (R), together with recovery of the original In<sub>2</sub>O<sub>3</sub>. The mechanism for the photocatalytic degradation of RB in our experiment was proposed as follows



Under visible light irradiation, photogenerated electrons in In<sub>2</sub>O<sub>3</sub> moved freely to the TiO<sub>2</sub>, meanwhile, the photogenerated holes were left in the valence band of In<sub>2</sub>O<sub>3</sub>.<sup>48,49</sup> Dissolved oxygen molecules react with the surface of the TiO<sub>2</sub> electrons ( $e^-$ ) to yield superoxide radical anions,  $\bullet\text{O}_2^-$ , which on protonation generate the hydroperoxy,  $\text{HO}_2\bullet$ , radicals, producing hydroxyl radical  $\text{OH}\bullet$ , which was a strong oxidizing agent to decompose the organic dye.<sup>50,51</sup>

## CONCLUSIONS

In summary, In<sub>2</sub>O<sub>3</sub>–TiO<sub>2</sub> heteroarchitectures fabricated via the electrospinning and solvothermal methods possessed higher photocatalytic activities than the pure TiO<sub>2</sub> and In<sub>2</sub>O<sub>3</sub> for the degradation of RB dye under visible light irradiation. Furthermore, the In<sub>2</sub>O<sub>3</sub>–TiO<sub>2</sub> heteroarchitectures nanofibers could be easily recycled without decrease of the photocatalytic activity due to their one-dimensional nanostructure property. And, it is expected that the In<sub>2</sub>O<sub>3</sub>–TiO<sub>2</sub> heteroarchitectures nanofibers with high photocatalytic activity will greatly promote their practical application to eliminate the organic pollutants from wastewater.

## AUTHOR INFORMATION

### Corresponding Author

\*E-mail: clshao@nenu.edu.cn (C.S.); chenb608@nenu.edu.cn (B.C.). Tel.: 8643185098803.

## ACKNOWLEDGMENTS

The present work is supported financially by the National Natural Science Foundation of China (50572014 and 50972027), and the Program for New Century Excellent Talents in University (NCET-05-0322).

## REFERENCES

- (1) Fujishima, A.; Honda, K. *Nature* **1972**, *238*, 37.
- (2) Wang, C.; Shao, C.; Liu, Y.; Li, X. *Inorg. Chem.* **2009**, *48*, 1105.
- (3) Ye, C.; Bando, Y.; Shen, G.; Golberg, D. *J. Phys. Chem. B* **2006**, *110*, 15146.
- (4) Zhang, L.; Wang, W.; Yang, J.; Chen, Z.; Zhang, W.; Zhou, L.; Liu, S. *Appl. Catal., A* **2006**, *308*, 105.
- (5) Li, L.; Chu, Y.; Liu, Y.; Dong, L. *J. Phys. Chem. C* **2007**, *111*, 2123.
- (6) Smith, Y. R.; Kar, A.; Subramanian, V. R. *Ind. Eng. Chem. Res.* **2009**, *48*, 10268.
- (7) Mu, J. B.; Shao, C. L.; Guo, Z. C.; Zhang, Z. Y.; Zhang, M. Y.; Zhang, P.; Chen, B.; Liu, Y. C. *ACS Appl. Mater. Interfaces* **2011**, *3*, 590.
- (8) Fujishima, A.; Rao, T. N.; Tryk, D. A. *J. Photochem. Photobiol. C* **2000**, *1*, 1.
- (9) Kamat, P. V. *Chem. Rev.* **1993**, *93*, 267.
- (10) Hoffmann, M. R.; Martin, S. T.; Choi, W.; Bahnemann, D. W. *Chem. Rev.* **1995**, *95*, 69.
- (11) Zhang, M. Y.; Shao, C. L.; Guo, Z. C.; Zhang, Z. Y.; Mu, J. B.; Cao, T. P.; Liu, Y. C. *ACS Appl. Mater. Interfaces* **2011**, *3*, 369.
- (12) Liu, Y.; Li, J.; Wang, M. J.; Li, Z. Y.; Liu, H. T.; He, P.; Yang, X. R.; Li, J. H. *Cryst. Growth Des.* **2005**, *5*, 1643.
- (13) Wang, G.; Wang, Q.; Lu, W.; Li, J. H. *J. Phys. Chem. B* **2006**, *110*, 22029.
- (14) Linsebigler, A.; Lu, G.; Yates, J. T. *Chem. Rev.* **1995**, *95*, 735.
- (15) Anpo, M.; Takeuchi, M. *J. Catal.* **2003**, *216*, 505.
- (16) Diebold, U. *Surf. Sci. Rep.* **2003**, *48*, 53.
- (17) Arana, J.; Diaz, O. G.; Saracho, M. M.; Rodriguez, J. M. D.; Melian, J. A. H.; Pena, J. P. *Appl. Catal., B* **2001**, *32*, 49.
- (18) Choi, W.; Termin, A.; Hoffmann, M. R. *J. Phys. Chem.* **1994**, *98*, 13669.
- (19) Wang, J. W.; Mao, B. D.; Gole, J. L.; Burda, C. *Nanoscale* **2010**, *2*, 2257.
- (20) In, S.; Orlov, A.; Berg, R.; Garcia, F.; Pedrosa-Jimenez, S.; Tikho, M. S.; Wright, D. S.; Lambert, R. M. *J. Am. Chem. Soc.* **2007**, *129*, 13790.
- (21) Sakthivel, S.; Kisch, H. *Angew. Chem., Int. Ed.* **2003**, *42*, 4908.
- (22) Valentin, C. D.; Pacchioni, G.; Selloni, A. *Chem. Mater.* **2005**, *17*, 6656.
- (23) Asahi, R.; Morikawa, T.; Ohwaki, T.; Aoki, K.; Taga, Y. *Science* **2001**, *293*, 269.
- (24) Zhang, L. W.; Fu, H. B.; Zhu, Y. F. *Adv. Funct. Mater.* **2008**, *18*, 2180.
- (25) Zhong, J.; Chen, F.; Zhang, J. L. *J. Phys. Chem. C* **2010**, *114*, 933.
- (26) Zhao, L.; Chen, X. F.; Wang, X. C.; Zhang, Y. J.; Wei, W.; Sun, Y. H.; Antonietti, M.; Titirici, M. M. *Adv. Mater.* **2010**, *22*, 3317.
- (27) Lettmann, C.; Hildenbrand, K. H.; Macyk, W.; Maier, W. F. *Appl. Catal., B* **2001**, *32*, 215.
- (28) Mitoraj, D.; Kisch, H. *Angew. Chem., Int. Ed.* **2008**, *47*, 9975.
- (29) Dong, F.; Guo, S.; Wang, H. Q.; Li, X. F.; Wu, Z. B. *J. Phys. Chem. C* **2011**, *115*, 13285.
- (30) Asahi, R.; Morikawa, T.; Ohwaki, T.; Aoki, K.; Taga, Y. *Science* **2001**, *293*, 269.
- (31) Quarto, F.; Sunseri, C.; Piazza, S.; Romano, M. *J. Phys. Chem. B* **1997**, *101*, 2519.
- (32) Lv, J.; Kako, T.; Li, Z. S.; Zou, Z. G.; Ye, J. H. *J. Phys. Chem. C* **2010**, *114*, 6157.
- (33) Wang, Z. Y.; Huang, B. B.; Dai, Y.; Qin, X. Y.; Zhang, X. Y.; Wang, P.; Liu, H. X.; Yu, J. X. *J. Phys. Chem. C* **2009**, *113*, 4612.
- (34) Chang, W. K.; Rao, K. K.; Kuo, H. C.; Cai, J. F.; Wong, M. S. *Appl. Catal., A* **2007**, *321*, 1.
- (35) Shchukin, D.; Poznyak, S.; Kulak, A.; Pichat, P. *J. Photochem. Photobiol. A* **2004**, *162*, 423.
- (36) Poznyak, S. K.; Talapin, D. V.; Kulak, A. I. *J. Phys. Chem. B* **2001**, *105*, 4816.
- (37) González, V. R.; Rodríguez, A. M.; May, M.; Tzompantzi, F.; Gómez, R. *J. Photochem. Photobiol., A* **2008**, *193*, 266.
- (38) Poznyak, S. K.; Talapin, D. V.; Anatoly, I. K. *Thin Solid Films* **2002**, *405*, 35.
- (39) Reddy, B. M.; Chowdhury, B.; Smirniotis, P. G. *Appl. Catal., A* **2001**, *219*, 53.
- (40) Yang, X.; Wang, Y.; Xu, L.; Yu, X.; Guo, Y. *J. Phys. Chem. C* **2008**, *112*, 11481.
- (41) Pujilaksono, B.; Klement, U.; Nyborg, L.; Jelvestam, U.; Hill, S.; Burgard, D. *Mater. Charact.* **2005**, *54*, 1.

- (42) Zschoerper, N.; Katzenmaier, V.; Vohrer, U.; Haupt, M.; Oehr, C.; Hirth, T. *Carbon* **2009**, *47*, 2174.
- (43) Gurlo, A.; Barsan, N.; Weimar, U.; Ivanovskaya, M.; Taurino, A.; Siciliano, P. *Chem. Mater.* **2003**, *15*, 4377.
- (44) Li, J. H.; Shen, D. Z.; Zhang, J. Y.; Zhao, D. X.; Li, B. S.; Lu, Y. M.; Liu, Y. C.; Fan, X. W. *J. Magn. Magn. Mater.* **2006**, *302*, 118.
- (45) Turchi, C.; Ollis, D. J. *Catal.* **1990**, *122*, 178.
- (46) Lee, M.; Park, S.; Lee, G.; Ju, C.; Hong, S. *Catal. Today* **2005**, *101*, 283.
- (47) He, T.; Ma, Y.; Cao, Y.; Hu, X.; Liu, H.; Zhang, G.; Yang, W.; Yao, J. *J. Phys. Chem. B* **2002**, *106*, 12670.
- (48) Zhang, H.; Lv, X. J.; Li, Y. M.; Wang, Y.; Li, J. H. *ACS Nano* **2010**, *4*, 380.
- (49) Li, J. H.; Zhang, J. Z. *Coord. Chem. Rev.* **2009**, *253*, 3015.
- (50) Aarthi, T.; Madras, G. *Ind. Eng. Chem. Res.* **2007**, *46*, 7.
- (51) Rajeshwar, K.; Osugi, M.; Chanmanee, W.; Chenthamarakshan, C.; Zannoni, M.; Kajitvichyanukul, P.; Krishnan, A. R. *Photochem. Photobiol. C* **2008**, *9*, 171.